Journal of Materials Chemistry A

ROYAL SOCIETY OF CHEMISTRY

PAPER

View Article Online
View Journal

Cite this: DOI: 10.1039/d6ta01059h

Decoupling the solubility of redox active species and the energy density of redox flow batteries using supersaturated, phase-change electrolytes

Jing Xie, [a] Shrihari Sankarasubramanian,[bc] Jeffrey G. Catalano [d] and Vijay Ramani *[a]

Redox flow batteries (RFBs), with their characteristic decoupling of power density and energy capacity, are scalable energy storage systems that can help smooth out the intermittency of solar and wind power on the electric grid. Among the many different redox couples considered in RFBs, the cerium (Ce) redox couple, Ce(IV)/Ce(III), is particularly attractive due to its high standard potential (1.61 V *vs.* standard hydrogen electrode, SHE) and the relative abundance of Ce in Earth's crust (as abundant as lead). Ce-based RFBs, such as the Zn–Ce system, have been scaled up and commercialized, but meeting ever-lower energy storage cost targets (<$50 kW h^{-1}) requires significantly higher Ce electrolyte energy density. Herein, in a departure from previous studies that utilize acid-supported Ce electrolyte solutions (*e.g.*, sulfuric acid), we have developed a new phase-change Ce electrolyte with ammonium sulfate (AS) as the supporting electrolyte. The solubility of Ce(IV) was enhanced to 1.23 M by optimizing the ratio between the Ce salt and AS. This ~40% increase in energy density was found to be a function of solution chemistry, with complementary effects of Ce(IV) hydrolysis with water and complexation with anions. This cost-effective Ce electrolyte was paired with the titanium (Ti) redox couple to demonstrate a high-energy-density, low-cost Ce-based RFB. During cycling, part of the Ce was precipitated to form a slurry in the electrolyte. This slurry was succesfully cycled and reoxidized to the more soluble Ce(IV) form. 20 cycles (75 minutes per cycle) of the phase-change Ti–Ce RFB was demonstrated with a final energy efficiency > 70%.

Received 3rd February 2026
Accepted 28th April 2026

DOI: 10.1039/d6ta01059h

rsc.li/materials-a

Introduction

Redox flow batteries (RFBs) have attracted significant attention due to their ability to decouple energy capacity from power output, making them ideal for large-scale energy storage systems.[1] While all-vanadium RFBs remain the most widely studied and applied, the high cost of raw materials and relatively low output potential drive forward the research on other redox couples.[2,3] In the meantime, the development of aqueous inorganic RFBs is usually limited by the poor solubility of active species. As the most abundant and inexpensive rare earth element,[4] cerium (Ce) has a broad range of applications, such as automotive catalysts,[5] wastewater treatment,[6] alloy synthesis,[7] and therapeutic agents.[8] The Ce redox couple, Ce(IV)/Ce(III), has been utilized in electrochemical energy storage due to its high redox potential.[9] More specifically, it has been successfully incorporated into aqueous RFBs working as the positive side[10] and has been coupled with Zn, Pb, H_2, V, and Ti to yield a variety of RFBs.[11] Zn–Ce RFB was even commercialized by Plurion before they shut down due to the 2008 economic crisis. To our best knowledge, in previous studies, Ce species were dissolved in traditional acidic supporting electrolytes to enhance stability and kinetics, with the Ce solubility limited to (at best) 0.9 M.[12,13] Ce solubility in sulfuric acid (H_2SO_4) has been shown to decrease as the acid concentration increases, which is usually explained by the "common ion effect",[14] while an inverse relationship between Ce(III) and Ce(IV) solubility could be seen in methanesulfonic acid (CH_3SO_3H).[15] Due to the limitation of Ce solubility in acidic electrolytes, the concentration of active species in aqueous RFBs using the Ce redox couple is usually below 1 M. Some reports exist of cerium redox in non-aqueous electrolytes, such as acetonitrile, but the very low solubility (0.05 M in this case[16]) makes these systems far from practical.

The study of solubility enhancement in aqueous inorganic RFBs is much more scarce compared to studies on organic actives,[17] and most of the existing research is focusing on vanadium (V) RFBs.[18] The group of Prof. Skyllas-Kazacos has

[a]*Department of Energy, Environmental & Chemical Engineering, Washington University in St. Louis, 1 Brookings Drive, South Brookings Hall, Room 135, St. Louis, MO, 63130, USA. E-mail: ramani@wustl.edu; Tel: +1-314-935-7924*

[b]*Department of Biomedical Engineering and Chemical Engineering, University of Texas at San Antonio, San Antonio, TX, 78429, USA*

[c]*Department of Mechanical, Aerospace and Industrial Engineering, University of Texas at San Antonio, San Antonio, TX, 78429, USA*

[d]*Department of Earth and Planetary Sciences, Washington University in St. Louis, St. Louis, MO, 63130, USA*

conducted a comprehensive study on the effects of different additives on supersaturated V electrolytes. They first proposed the idea of using "stabilizing agents" that do not promote V solubility but postpone precipitation by adsorbing to the nucleation sites to inhibit crystal growth.[19] According to their research, the ammonium (NH_4^+) and phosphate (PO_4^{3-}) ions were shown to work best as precipitation inhibitors.[20] Unlike this study, the amount of effective additives in their studies was very low (*e.g.*, 1 to 5 wt%), which makes complexing an unlikely mechanism because it requires a comparable concentration between metal ions and complexing agents.

Building on our success developing the titanium (Ti)–Ce RFBs utilizing methanesulfonic acid as the supporting electrolyte and aiming to break through the existing Ce solubility limitation, we screened a series of non-acidic supporting electrolytes, and a solution of ammonium sulfate (AS) was found to enable Ce(IV) solubility as high as 1.23 M. Unlike prior studies where trace amounts of additives were added into conventional acidic electrolytes, AS is the only component of the electrolyte here apart from the dissolved Ce salt. Due to the high charge-to-radius ratio of Ce(IV), it easily hydrolyses with water when the solution pH is relatively high.[21] The near-neutral environment of the AS solution favors Ce(IV) hydrolysis and the release of protons, thus reducing the pH. The resultant low-pH environment drives the protonation of the Ce counterion sulfate (SO_4^{2-}) to form bisulfate (HSO_4^-), and the complexation between Ce(IV) and HSO_4^- tends to form a stable structure where the ratio of Ce(IV) to HSO_4^- is 1 : 3.[22] The synergistic effect of Ce(IV) hydrolysis, the resultant pH reduction, and the formation of bisulfate anions, enabling favorable complexation, serves as the foundation for our supersaturated electrolyte. This new Ce(IV) electrolyte was paired with the same concentration of Ti in AS, leading to a new type of RFB. Upon cycling, the Ce(III) ion exhibited much lower solubility compared to Ce(IV) and precipitated out of solution, but we were able to circulate the resultant slurry through the RFB and convert the Ce(III) back to dissolved Ce(IV). This phase-change cycling was carried out for 20 cycles with no irreversible capacity fade and an energy efficiency (EE) higher than 70% at 50 mA cm^{-2} operating current density. Thus, we demonstrated a new Ce-based, slurry aqueous inorganic RFB with a theoretical energy density of 33 Ah L^{-1}.

Materials and methods

Chemicals

$Ce(SO_4)_2 \cdot xH_2O$ (Alfa Aesar, 98%), $TiOSO_4$ (Sigma-Aldrich, 34%), and $VOSO_4$ (Sigma-Aldrich) were used as the raw Ce(IV), Ti(IV), and V(IV) materials, respectively. H_2SO_4 (Sigma-Aldrich, 99%) and CH_3SO_3H (Sigma-Aldrich, 99%) were used as the supporting electrolytes. The original Ce(IV), Ti(IV), and V(IV) solutions were prepared by first dissolving the required amount of AS in deionized water, then adding the corresponding amount of metal salt into the AS solution. A stirring bar was used to speed up the dissolution.

Characterization methods

Ce L_{III}-edge X-ray absorption near-edge structure (XANES) spectra were obtained using an easyXAFS 300+ X-ray spectrometer.[23] The second harmonic of a spherically-bent Ge(211) crystal was used to select the incident beam energy, which was detected using a silicon drift detector. $Ce(SO_4)_2$ dissolved in AS solution was injected into a sample cell consisting of a 0.25 mm thick PTFE ring shim (25.4 mm outer diameter, 15.9 mm inner diameter) sealed on both sides with Kapton tape. CeO_2 and $Ce_2(SO_4)_3$ were ground in a mortar and pestle, spread as a uniform layer on cellulose tape, and then stacked in six layers for measurement to optimize absorbance. Data were collected in transmission mode with the energy calibrated using a Cr metal foil, and the first inflection point of the Cr K-edge set to 5989 eV. The spectrum of $Ce(SO_4)_2$ was obtained from the XAS Database at the Canadian Light Source (https://xasdb.lightsource.ca, sample ID: id12345). Data were calibrated and normalized in the Athena[24] interface to IFEFFIT.[25] Raman spectroscopy was performed using a Renishaw inVia confocal Raman spectrometer equipped with a 514 nm laser excitation source. The laser power at the sample surface was set to 2 mW, and spectra were obtained by focusing the laser beam on the surface plasmon-coupled emission (SPCE) working electrode using a 50× objective lens with a numerical aperture of 0.9 and an exposure time of 30 s. Ultraviolet-visible spectroscopy (UV-Vis) was conducted using a Varian Cary 50Bio. The absorption spectra were obtained between 190 and 1100 nm at a scan rate of 600 nm min^{-1}. A quartz cuvette with a path length of 10 mm was used, and the supporting electrolyte solution without Ce(IV) was used to do baseline correction before running each sample.

Electrochemical measurements

Cyclic voltammetry (CV) was conducted using WaveNowXV Potentiostat Bundles (PINE Research). A three-electrode setup was used for the measurements: carbon paper (CP, AvCarb MGL190, Fuel Cell Store) or carbon felt (CF, GFA 6, SGL Group) with a 1 cm^2 surface area as the working electrode, Ag/AgCl as the reference electrode, and platinum wire as the counter electrode. The potential window of CV was 0 to 2 V *vs.* Ag/AgCl, and different scan rates (*e.g.*, 2.5, 5, 7.5, and 10 mV s^{-1}) were selected for further calculation. The results were analyzed using the Nicholson–Shain (N–S) and Klinger–Kochi (K–K) equations to obtain the diffusion coefficient (D_0) and standard reaction rate constant (k_0).[26–28] More details for the calculation process are provided in the Results and discussion section.

Redox flow battery tests

All tests were conducted using an 857 Redox Flow Cell Test System (Scribner). CF with a 6 mm thickness was cut into a 5 × 5 cm segment, leading to a 25 cm^2 surface area. Raw and heat-treated (500 °C, 8 h, air atmosphere) CF were used as the positive (Ce) and negative (Ti) side electrodes, respectively. The separator was a quaternized cardo-poly(ether ketone)-based anion-exchange membrane functionalized with

trimethylamine (QPEK-C-TMA AEM), developed by our group; the synthesis details are provided in previous studies.[29] A serpentine-type flow field with enlarged inlet and outlet was used, as shown in SI Appendix, Fig. S1. A total of 50 mL of electrolyte was used for each side. Since the original Ce(IV) and Ti(IV) electrolytes were in fully charged and discharged states, respectively, a V–Ti RFB was assembled by pairing V(IV) and Ti(IV) electrolytes and a single, full charge was operated at 50 mA cm^{-2} until the cell reached cut-off potential (2 V) to obtain a fully charged Ti electrolyte, which contains mostly Ti(III). Next, this Ti electrolyte was paired with the Ce(IV) electrolyte for the cycling test in a sequence of discharge followed by charge–discharge. More details about the electrolyte composition and test protocol are provided in the SI Appendix.

Results and discussion

Determination of Ce(IV) electrolyte composition

Solutions of different chemicals containing NH_4^+, PO_4^{3-}, or $-NH_2$ were screened for their effects on $Ce(SO_4)_2$ solubility as shown in Table 1. The AS solution was the only candidate that had a positive effect on Ce(IV) solubility, with the solubility of Ce(IV) in other solutions being even lower than that in pure water. It was apparent that both NH_4^+ and SO_4^{2-} play a role in promoting Ce(IV) solubility, as the substitution of either would disable the effect (*e.g.*, both Na_2SO_4 and NH_4Cl solutions, resulting in poor Ce(IV) solubility). In optimizing the $Ce(SO_4)_2$ and AS system, the ratio of NH_4 to SO_4 was varied and found to have a significant impact on Ce(IV) solubility, as shown in Table 2. Note that we have used NH_4 and SO_4 instead of NH_4^+ and SO_4^{2-} to denote all different species of ammonium (*e.g.*, NH_3 and NH_4^+) and sulfate (*e.g.*, SO_4^{2-} and HSO_4^-) in solution. The optimum ratio of NH_4 to SO_4 was determined to be 0.6 and this resulted in the highest observed Ce(IV) solubility of 1.23 M. Moreover, it is noteworthy that when the ratio of NH_4 to SO_4 was fixed (*i.e.*, at 0.6 : 1), the Ce(IV) solution remained stable only when the Ce(IV) content reached a relatively high level (solutions 1 and 4, solutions 5 to 8, Table 2). The mechanism of this phenomenon is further discussed.

Table 1 Effects of different supporting electrolytes on the $Ce(SO_4)_2$ solubility[a]

Additive	Effect	Ce(IV) conc.[a] (M)
$(NH_4)_2SO_4$	+	1.23
H_2SO_4	−	0.5
H_3PO_4	−	—
Na_2SO_4	−	—
CF_3SO_3H	−	—
$Ce(NH_4)_4(SO_4)_4$	−	0.1
NH_4Cl	−	—
CH_3COONH_4	−	—
NH_4SCN	−	—
$(NH_4)_2S_2O_8$	−	—
$NH_4SO_3NH_2$	−	—

[a] The "−" sign in the Ce(IV) concentration column indicates that for the given type of supporting electrolyte, the lowest amount of $Ce(SO_4)_2$ in the dissolution experiment was not able to fully dissolve.

Physicochemical characterization

The XANES spectrum of 1.23 M $Ce(SO_4)_2$ in 1.05 M AS (Fig. 1A) displayed white-line peaks at 5730.0 and 5737.5 eV, consistent with Ce(IV). The peak at 5737.5 eV had greater intensity than at 5730 eV, similar to solid $Ce(SO_4)_2$ and distinct from CeO_2. The peak intensity ratio of CeO_2 is similar for crystalline and amorphous forms,[30,31] as well as $Ce(OH)_4$,[32] consistently distinct from Ce(IV) in the electrolyte solution, which also had a more pronounced pre-edge feature at 5720 eV and lacked the shoulder at 5726.5 eV found in CeO_2 (SI Appendix, Fig. S2A). The intensity minimum at 5732.5 eV was deeper for $Ce(SO_4)_2$ dissolved in AS compared to solid $Ce(SO_4)_2$ (SI Appendix, Fig. S2B), similar to what is reported for dissolved 0.1 M Ce(IV) in 2 M H_2SO_4.[33] The spectrum of $Ce(SO_4)_2$ dissolved in AS is clearly distinct from the trivalent sulfate, $Ce_2(SO_4)_3$ (SI Appendix, Fig. S2C). A linear-combination fit of the XANES spectrum of 1.23 M $Ce(SO_4)_2$ in 1.05 M AS to the spectra of the standards yielded 99.1% ± 0.4% $Ce(SO_4)_2$ and 0.9% ± 0.4% $Ce_2(SO_4)_3$, demonstrating that cerium in solution is predominantly >99% Ce(IV) (SI Appendix, Fig. S2D). The small Ce(III) component may be a fitting artifact needed to account for the spectral differences between dissolved and solid-phase $Ce(SO_4)_2$, as was previously observed.[33] This demonstrated that Ce(IV) dissolved in AS electrolyte occurs in a similar coordination state to that in a H_2SO_4 electrolyte and did not form oxide or hydroxide phases. Raman spectra for different Ce(IV) and blank solutions are shown in Fig. 1B. The original spectra were normalized based on the peak intensity of the silicon wafer, which occurred at 520 cm^{-1}. A totally symmetric ν_1-SO_4^{2-} peak located at around 980 cm^{-1}, representing unassociated SO_4^{2-}, was observed for the blank AS solution, which is consistent with previous literature, indicating that the AS solution is an ideal model for a "free" sulfate system.[34] After $Ce(SO_4)_2$ was dissolved in AS, the ν_1-SO_4^{2-} peak intensity decreased and completely disappeared at higher $Ce(SO_4)_2$ concentrations, and no HSO_4^--related peak was generated, indicating an interaction between sulfate and Ce^{4+}. Another bending mode, ν_4-SO_4^{2-}, located at 615 cm^{-1} in AS solution, showed a significant blueshift to 665 cm^{-1}, as presented in Fig. 1B. A previous study on supersaturated $MgSO_4$ solution has shown that a similar blueshift is related to the formation of contact ion pairs (CIPs).[35] This finding implies that instead of the total sulfate species concentration, an efficient binding between sulfate species and Ce(IV) is essential for obtaining a supersaturated Ce(IV) solution. On the other hand, when the concentration of $Ce(SO_4)_2$ was fixed at 0.123 M and the supporting electrolyte was varied, the ν_1-SO_4^{2-} peak intensity of $Ce(SO_4)_2$ in AS solution was most prominent, indicating a higher degree of free SO_4^{2-} (ESI Appendix, Fig. S3). The spectrum of $Ce(SO_4)_2$ in H_2SO_4 was nearly identical to that of H_2SO_4, which presented no ν_1-SO_4^{2-} peak but a tiny HSO_4^- peak at around 1047 cm^{-1}. Neither free SO_4^{2-} nor HSO_4^- was present when $Ce(SO_4)_2$ was dissolved in water, indicating a strong interaction between sulfate and Ce(IV). The fact that the

Table 2 Effects of the ratio of the ammonium and sulfate on the Ce(IV) electrolytes

Solution #	Ratio of NH_4 to SO_4	Nominal[a] Ce(IV) conc. (M)	Condition
1	0.6 : 1	1.4	Dissolved and stable for 21 days
2	0.55 : 1	1.4	Not dissolved
3	0.65 : 1	1.4	Not dissolved
4	0.6 : 1	1	Dissolved and precipitated within 1 day
5	1 : 1	0.1	Not dissolved
6	1 : 1	0.2	Not dissolved
7	1 : 1	0.3	Not dissolved
8	1 : 1	0.4	Dissolved
9	1.82 : 1	0.05	Dissolved and precipitated within 1 day

[a] The nominal concentration indicates the concentration before accounting for the volume expansion during the dissolution process. Unlike conventional solution preparation, which utilizes a volumetric flask, we only used a beaker to facilitate the dissolution. On the other hand, a volumetric flask requires that the initial solution volume be smaller than the target number when transferring into the flask, and even this small amount of water might result in a discrepancy in the solubility limitation. In that case, we first calculated the required amount of AS and $Ce(SO_4)_2$ for an expected volume (*e.g.*, 1.4 M Ce in 100 mL solution), then added the amount of water that was just enough to dissolve everything, then the final solution volume (114 mL) was measured and the actual concentration recalculated: $1.4 \times 100/114 = 1.23$ M.

solubility of $Ce(SO_4)_2$ in water was limited (less than 0.7 M) suggests that the complex stability is highly sensitive to the structure. The UV-vis spectra of Ce(IV) in AS and H_2SO_4 are depicted in Fig. 1C, where the Ce(IV) concentration had to be diluted about 1000-fold to obtain clear absorption peaks. With a significant difference in pH value (3.71 in AS *vs.* −0.02 in H_2SO_4), a clear redshift of the absorption peak from 272 to 317 nm was found after AS was substituted by H_2SO_4. A consistent redshift was observed when the supporting electrolyte consisted of different ratios of AS and H_2SO_4 (Fig. 1D). Likewise, Ce(IV) was found to be complexed more strongly with sulfate species in H_2SO_4 than methanesulfonate in CH_3SO_3H, with an absorption peak of 320 *vs.* 210 nm,[33] indicating a stronger complexation with a shift toward longer wavelength. In Fig. 1D, as the ratio between AS and H_2SO_4 decreased from infinity (only AS) to zero (only H_2SO_4), the pH was lowered while the sulfate species concentration was fixed. The redshift suggests that the binding affinity between Ce(IV) and the sulfate species is higher in a low-pH environment.

Ce(IV) hydrolysis and complexation

The complexation between Ce and anions, especially in acidic supporting electrolytes, has been studied extensively.[36–38] In some recent studies, it has been found that in H_2SO_4, Ce(IV) tends to complex with HSO_4^- and the dominant structure is $[Ce(IV)(H_2O)_6(HSO_4)_3]^+$.[22] In aqueous solutions containing sulfate species, the speciation relationship between SO_4^{2-} and HSO_4^- is influenced by the dissociation equilibrium constants of H_2SO_4, and HSO_4^- is the dominant species when the pH is low, *i.e.*, the dissociation of the first proton in H_2SO_4 is normally considered complete, but that of the second one is sluggish (SI Appendix, Section S2.1). Thus, a stable structure is obtained by the complexation between Ce(IV) and HSO_4^- instead of SO_4^{2-}, whose quantity is negligible. In AS solutions, however, SO_4^{2-} would be the dominant species rather than HSO_4^- due to the much higher pH (5.4) of the solution, and proton dissociation from NH_4^+ is unfavorable under neutral and acidic environments (SI Appendix, Section S2.2). As tabulated in the SI Appendix, Table S1, the pH of the AS solution decreased significantly after $Ce(SO_4)_2$ was dissolved, ensuring that most of the SO_4^{2-} ions were protonated to form HSO_4^-. The cause of this dramatic pH reduction upon $Ce(SO_4)_2$ dissolution was further examined.

The hydrolysis of Ce(IV) in aqueous solution is considered to be very strong.[39] In an ideal solution where the anions do not complex with Ce(IV), the general reaction for Ce(IV) hydrolysis with water is as follows:

$$Ce^{4+} + iH_2O \leftrightarrow Ce(OH)_i^{4-i} + iH^+, \quad (1)$$

where i is the hydration level with values between 0 and 4. The corresponding equilibrium constant, K_i, is defined as follows:

$$K_i = \frac{\left[Ce(OH)_i^{4-i}\right][H^+]^i}{\left[Ce^{4+}\right]}. \quad (2)$$

Using the values from previous literature,[40,41] the speciation abundance of different Ce(IV) compounds as a function of pH was generated (SI Appendix, Section S2.3 and Fig. S5). At higher pH, the hydrolysis of Ce(IV) is more prominent, indicating that it should be considered when AS is used as the supporting electrolyte. The Ce(IV) structure (*e.g.*, $[Ce(IV)(H_2O)_6(HSO_4)_3]^+$) proposed in previous studies did not consider this hydrolysis reaction, which could be explained by the following: (1) the pH of the supporting electrolyte used in those studies were low enough to retard Ce(IV) hydrolysis; (2) the Ce(IV) concentration used was very low (*e.g.*, 0.25 mM), making it unnecessary to account for the pH change caused by Ce(IV) hydrolysis.[22] In our study, however, the Ce(IV) concentration and the corresponding pH change indicated that a significant amount of Ce(IV) hydrolysis was taking place in the solution. When AS was the only supporting electrolyte, all protons were released by Ce(IV), and the number of protons released by each Ce(IV) was calculated from pH, Ce(IV), and sulfate concentration. Taking the electrolyte with the highest Ce(IV) concentration as an example, *i.e.*, 1.23 M $Ce(SO_4)_2$ in 1.05 M AS, the concentration of total protons was calculated as follows:

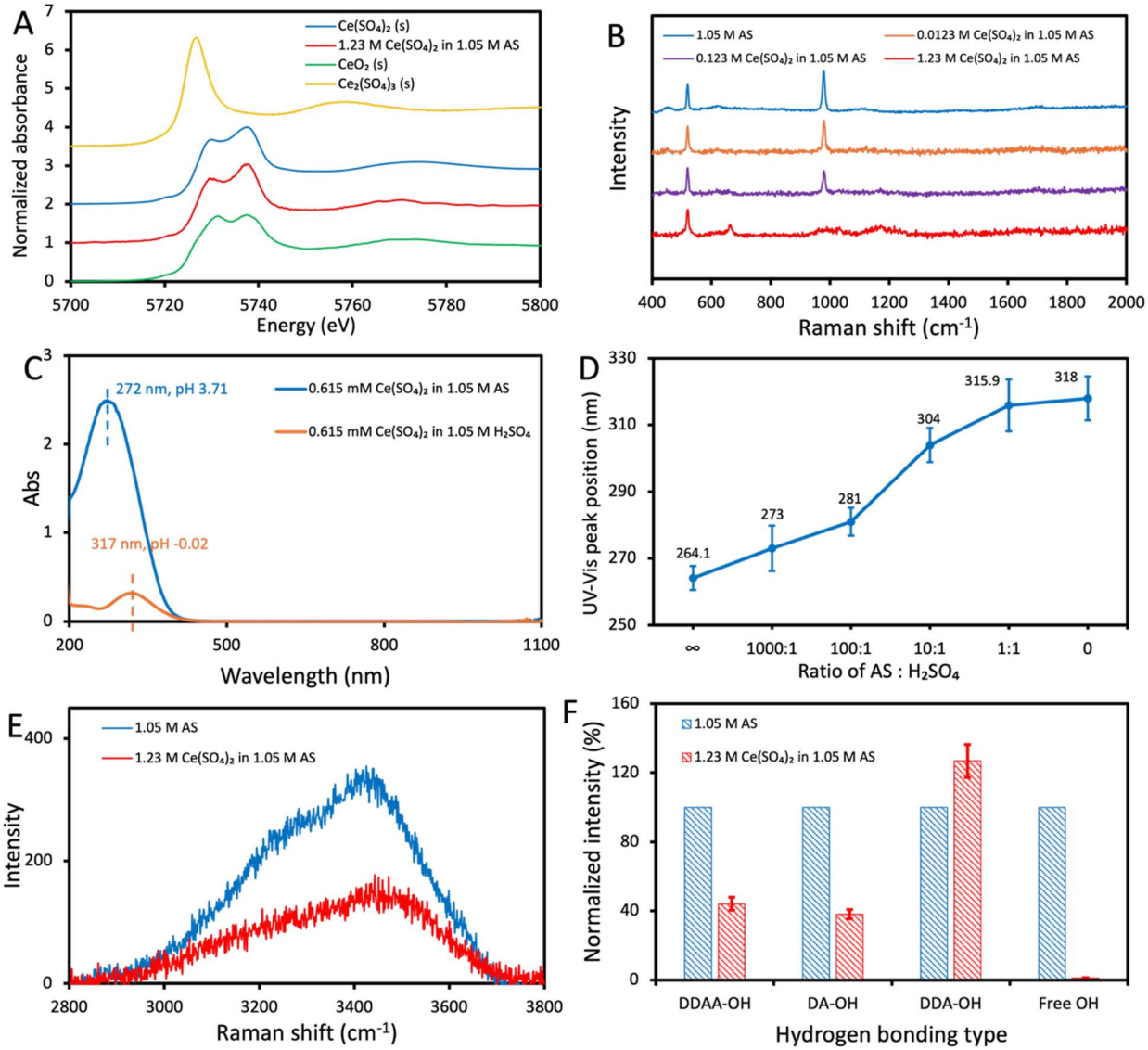

Fig. 1 (A) Ce L_{III}-edge XANES spectra of 1.23 M $Ce(SO_4)_2$ in a 1.05-M AS solution compared with the $Ce(SO_4)_2$, $Ce_2(SO_4)_3$ and CeO_2 standards. (B) Low-frequency Raman spectra of different concentrations of $Ce(SO_4)_2$ in 1.05 M AS. (C) UV-vis spectra of 0.615 mM $Ce(SO_4)_2$ in AS and H_2SO_4. (D) UV-vis absorption peak of 0.3075 mM $Ce(SO_4)_2$ in solutions with different ratios of AS to H_2SO_4 (SA). (E) High-frequency Raman spectra of 1.05 M AS and 1.23 M $Ce(SO_4)_2$ in 1.05 M AS. (F) Plots of intensity *vs.* hydrogen bonding type after 1.23 M $Ce(SO_4)_2$ was dissolved in 1.05 M AS.

$$\text{TOT } H^+ = \text{TOT } SO_4 + 10^{-pH_2} - 10^{-pH_1} = 4.955 \text{ M}, \quad (3)$$

where pH_1 (5.4) and pH_2 (−0.16) represent pH values before and after $Ce(SO_4)_2$ dissolution, and the term TOT SO_4 represents the protons captured by SO_4^{2-} to form HSO_4^- because the latter is the dominant sulfate species at such a low pH. Then, two ratios could be easily obtained as follows:

$$\frac{\text{TOT } H^+}{\text{TOT Ce(IV)}} = 4.03 \approx 4. \quad (4)$$

$$\frac{\text{TOT } SO_4}{\text{TOT Ce(IV)}} = 2.85 \approx 3. \quad (5)$$

The first ratio indicates that for each Ce(IV), four protons were released due to hydrolysis. The second ratio indicates that a complex could be attained where the ratio of Ce(IV) to HSO_4^- (following SO_4^{2-} protonation after Ce(IV) hydrolysis) is three, which coincides with a previous investigation.[22] The occurrence of strong hydrolysis with water is supported by the Raman spectral signals at high Raman shift, indicating OH vibrations and hydrogen bonding in water molecules. As shown in Fig. 1E, in the Raman shift range between 2800 and 3800 cm^{-1}, the overall intensity after $Ce(SO_4)_2$ dissolution was significantly lower than that of the AS solution. In this range, the Raman spectrum of water can be deconvoluted into five bands centered at 3004, 3227, 3431, 3565, and 3633 cm^{-1}, respectively (details in the SI Appendix, Section S2.4).[42] However, it has been reported that NH_4^+ presents two stretching bands at 3061 and 3131 cm^{-1}.[43] Since the percentage of water hydrogen bonding at 3004 cm^{-1} (single donor–double acceptor, DAA) is very small,

the deconvolution was still performed based on all five bands, but the quantitative comparison was made by excluding the band at 3004 cm^{-1}. The deconvoluted results are shown in the SI Appendix, Fig. S6, and the intensities of four other types of hydrogen bonding were normalized based on the peak area of the AS solution, as illustrated in Fig. 1F. The intensities of the double donor–double acceptor (DDAA, 3227 cm^{-1}) and single donor–single acceptor (DA, 3431 cm^{-1}) were reduced to less than 50%, and that of free OH vibrations (3633 cm^{-1}) was nearly eliminated. The notable decrease in hydrogen bonding intensity indicates that water molecules are more structured by hydrolysis and complexation. Hence, we propose a new pathway for Ce(IV) dissolution and complexation in AS solutions that combines both hydrolysis with water and complexation with HSO_4^-, to form the possible complex $[Ce(OH)_4(HSO_4^-)_3]^{3-}$, as depicted in Fig. 2. The bonding strength between Ce(IV) and HSO_4^- becomes weaker due to the negative charge carried by the hydroxide (OH^-) ions, reducing the likelihood of Ce(IV)–sulfate precipitation and thus increasing Ce(IV) solubility. Similar calculations and analysis were performed on all three supporting electrolytes (water, H_2SO_4, and AS) with a lower Ce(IV) concentration (0.123 M) (SI Appendix, Section S2.5). In water, the ratio of Ce to sulfate was fixed at 1 : 2, suggesting that the stable structure, which requires a ratio of 1 : 3, was never achieved. As a result, the solution would tend to precipitate relatively quickly, as shown in the SI Appendix, Fig. S7. In H_2SO_4, the majority of total protons came from the acid itself instead of Ce(IV) hydrolysis, revealing that hydrolysis was thermodynamically unfavorable. At a relatively low concentration (*e.g.*, 0.123 M Ce), the sulfate from $Ce(SO_4)_2$ could be fully protonated by H_2SO_4 and Ce(IV) hydrolysis, leading to the formation of stable Ce(IV) complex structures (the ratio of sulfate to Ce is much higher than 3). As the concentration of $Ce(SO_4)_2$ or H_2SO_4 is increased, however, free SO_4^{2-} starts to be non-negligible in the system, which competes with HSO_4^- to bind with Ce(IV) and precipitate as $Ce(SO_4)_2$ solid. This is a manifestation of the common-ion effect, wherein the solubility of $Ce(SO_4)_2$ decreases as the H_2SO_4 concentration increases.[14] Notably, the calculation results for 0.123 M $Ce(SO_4)_2$ in 1.05 M AS suggest that eight protons were released, much higher than the highest number from hydrolysis with water (four). Thus, at this intermediate Ce(IV) concentration, NH_4^+ can be hydrolyzed by Ce(IV) to release protons and a complex with $-NH_3$ can be formed. The participation of NH_4^+ supports the earlier observation that the same concentration of $Ce(SO_4)_2$ was not able to dissolve in Na_2SO_4. The presence of free SO_4^{2-} in this solution (pH = 1.63) implies that the solution was not stable and would precipitate, and this was indeed observed experimentally as shown in the SI Appendix, Fig. S8. At even higher Ce(IV) concentrations (1.23 M), the protons from water hydrolysis were abundant and ammonium was re-protonated and detached. Based on the analysis above, a low pH environment that results in HSO_4^- being the dominant species of sulfate is key for a stable $Ce(SO_4)_2$ solution. Ce(IV) concentration and stability were found to be a function of the pH, and increase at low pH, but only if the acidity is generated by Ce(IV) hydrolysis instead of the addition of any acidic supporting electrolyte. Thus, the improved solubility is a result of the complementary and synergistic effects of Ce(IV) hydrolysis and complexation. We, herein, propose a new criterion for $Ce(SO_4)_2$ solubility in aqueous solution: the sulfate content does not decide the solubility, but a favorable complex between Ce(IV) and other species (*i.e.*, water and HSO_4^-) plays the key role. The low pH of the final solution is a prerequisite since it makes sure that HSO_4^- is the dominant sulfate species, but the low pH should come from Ce(IV) hydrolysis (*e.g.*, in AS) to form $Ce(OH)_i^{4-i}$ intermediates, and not the solvent itself (*e.g.*, H_2SO_4). A more quantitative study (*e.g.*, density functional theory calculation and extended X-ray absorption fine structure) will be conducted in our future work to prove the Ce(IV) complex coordination.

Electrochemical characterization

In this study, CP and CF were selected as candidates for electrodes on the Ce side. In our previous study,[51] CF was proven to be degraded by the methanesulfonic acid-based Ce(IV) electrolyte, shown by the vanishing of the anodic peak and shifting of the cathodic peak towards the negative direction after CF was immersed in the Ce electrolyte for 24 h. A similar stability test was conducted in this study. The CVs revealed that with the AS supporting electrolyte, both peak positions and redox currents

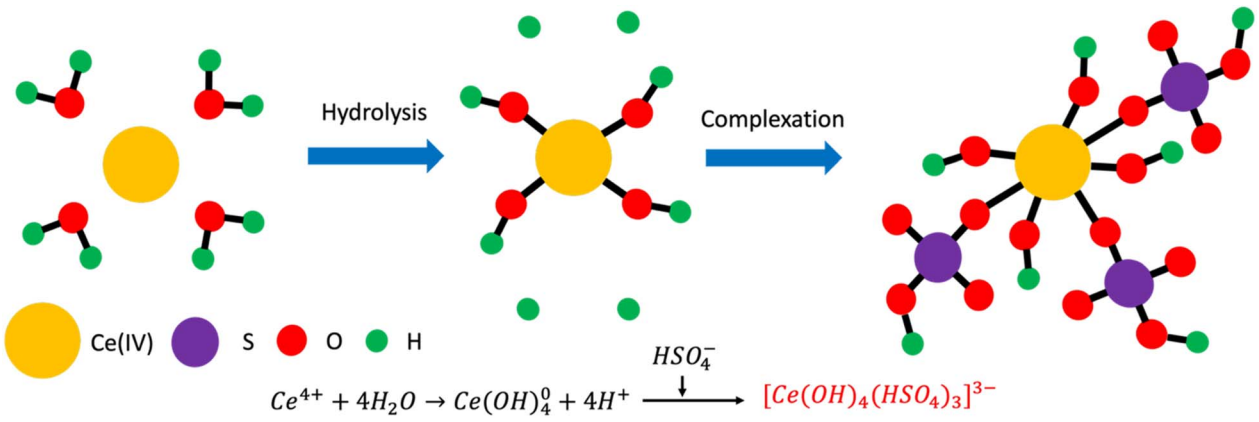

Fig. 2 Schematic of the Ce(IV) hydrolysis and possible complexation coordination in an AS solution.

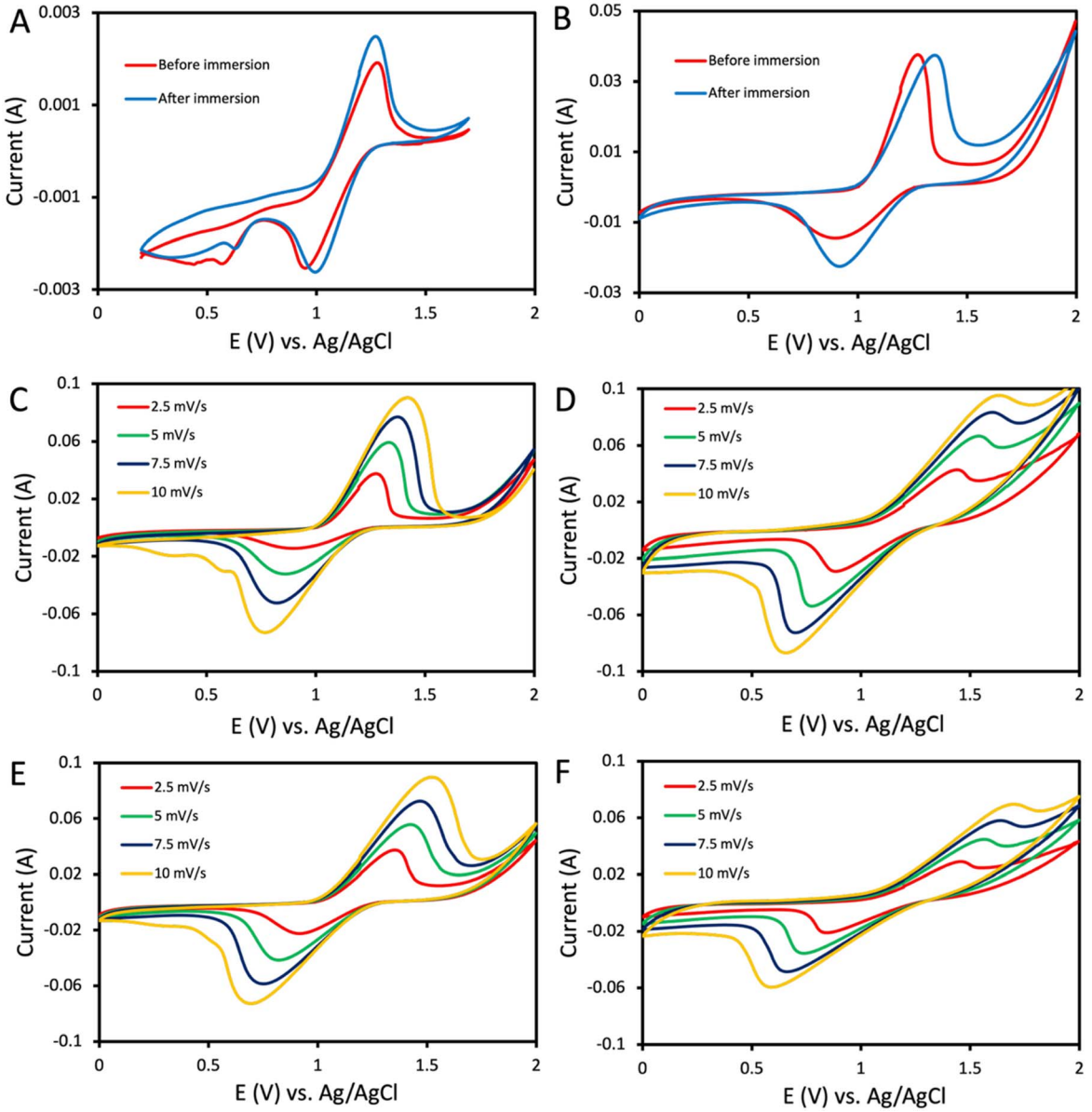

Fig. 3 CV plots of different carbon electrodes with 0.123 M $Ce(SO_4)_2$ in 1.05 M AS: (A) CP before and after immersion at 2.5 mV s^{-1}; (B) CF before and after immersion at 2.5 mV s^{-1}; (C) CF before immersion; (D) HT CF before immersion; (E) CF after immersion; and (F) HT CF after immersion.

on CF electrodes remained stable after immersion in the Ce(IV) electrolyte for 24 h, as shown in Fig. 3B. The decrease in the oxidizing nature of Ce(IV) in AS (compared with the CH_3SO_3H supporting electrolytes) was attributed to the stronger complexation with sulfate species and hydrolysis with water, which made Ce(IV) more stable and harder to be reduced chemically. The comparison between the CVs of CP and CF in Fig. 3A and B and the SI Appendix, Table S2 demonstrates significant performance differences: better reversibility on CP (smaller peak separation) and enhanced reactivity on CF (higher peak currents).[44] The improved apparent kinetics on CF is attributed to its higher surface area, while the increased reversibility on CP is attributed to differences in surface functionalization (additional fundamental studies are needed, but are outside the scope of this study). Similarly, raw CP and HT CP, raw CF and HT CF were immersed in the Ce(IV)–AS electrolyte, and both anodic and cathodic peak currents dropped significantly for HT CF, indicating poor oxidative stability, as depicted in Fig. 3D and F. We hypothesize that the deterioration of HT CF in the Ce(IV) electrolyte was facilitated by the oxygen functional groups produced on the surface during thermal pretreatment. Based on these results, CF was selected as the electrode for the Ce side.

The CVs of CF at different scan rates were analyzed to obtain the diffusion coefficients of the Ce complexes and the reaction rate constants. As shown in Fig. 3C, the peak potential separations at all scan rates were higher than 59 mV and increased with scan rate, suggesting that the Ce redox reaction was not readily reversible.[45] The N–S equation was used to calculate D_0 as follows:

$$i_p = 2.99 \times 10^5 n^{3/2} \alpha^{1/2} A C_0 D_0^{1/2} \nu^{1/2} \quad (6)$$

where i_p is the peak current, n is the number of electrons transferred during the reaction, α is the electron transfer coefficient, A is the electrode surface area, C_0 is the Ce concentration in bulk electrolyte, D_0 is the diffusion coefficient, and ν is the scan rate.[26,27] The transfer coefficient, α, was calculated using the following equation:

$$\alpha = \frac{1.86RT}{F(E_p - E_{p/2})}, \quad (7)$$

where R is the universal gas constant (8.314 J mol^{-1} K^{-1}), T is the temperature, F is Faraday's constant (96 485 C mol^{-1}), E_p is the peak potential, and $E_{p/2}$ is the half-peak potential.[46] The α values are tabulated in the SI Appendix, Table S3, and a clear deviation from 0.5 indicates that the reaction is irreversible. Similarly, the K–K equation was used for obtaining k_0 as follows:

$$k_0 \exp\left[\frac{\alpha n F}{RT}(E_p - E_0)\right] = 2.18\left[\frac{D_0 \alpha n F \nu}{RT}\right]^{\left(\frac{1}{2}\right)}, \quad (8)$$

where k_0 is the standard rate constant, E_0 is the standard electrode potential, which was calculated from the average of cathodic and anodic peak potentials. The corresponding N–S and K–K plots are depicted in the SI Appendix, Fig. S9, from which the slope was used to calculate the value of D_0 and k_0, as tabulated in the SI Appendix, Table S4.

Ti–Ce RFBs test

The optimized Ce electrolyte was tested on CF electrodes in a Ti–Ce RFB. First, the Ti electrolyte was reduced to Ti(III) in a V–Ti cell configuration to enable us to cycle it with Ce(IV). The theoretical time for a single full charge of the V–Ti RFB was calculated to be 1.32 h, which was close to the actual duration (1.2 h), suggesting that all Ti(IV) was reduced to Ti(III) (ESI Appendix, Section S2.6). The QPEK-C-TMA AEM utilized in this study has been applied to several RFB systems with Ce, Ti, and V,[12,51–53] and the permselectivity was proven to be excellent without unwanted crossover. The high-frequency resistance (HFR), which includes ionic or contact resistance of different components in RFB,[47] is shown in Fig. 4A for the initial stage of Ti–Ce RFBs cycling. A significant fluctuation of HFR during discharge was observed with a peak value higher than 500 mΩ at the beginning of the discharge process. To put this in perspective, the HFR in all-V RFB cells is typically around 50 mΩ; thus, it is not a major performance limiter.[48,49] When a constant-current plus constant-voltage protocol was used, the large ohmic polarization in the early phase of discharge would bring the cell potential to the cut-off condition immediately, forcing the system into the next constant-voltage stage and lowering the energy efficiency (EE) (Fig. 4B). As the discharge proceeded, however, the HFR decreased to a more reasonable level (100 mΩ), which led to a remarkable phenomenon: the discharge current density in the constant-voltage phase was promoted to more than two times that of the constant-current stage (50 mA cm^{-2}), indicating that significant discharge capacity was not utilized in the constant current (CC) stage (Fig. 4C). The hypothesis that this pronounced HFR was due to the precipitation of nanoparticles of Ce(III) stemmed from the low solubility of Ce(III) in sulfate environment being incorrect, as the HFR was not affected by increases in flowrate that would be expected to sweep away particulate precipitates inside the cell (see HFR as a function of electrolyte flowrate in SI Appendix Fig. S11). The conductivity of both Ce and Ti electrolytes is

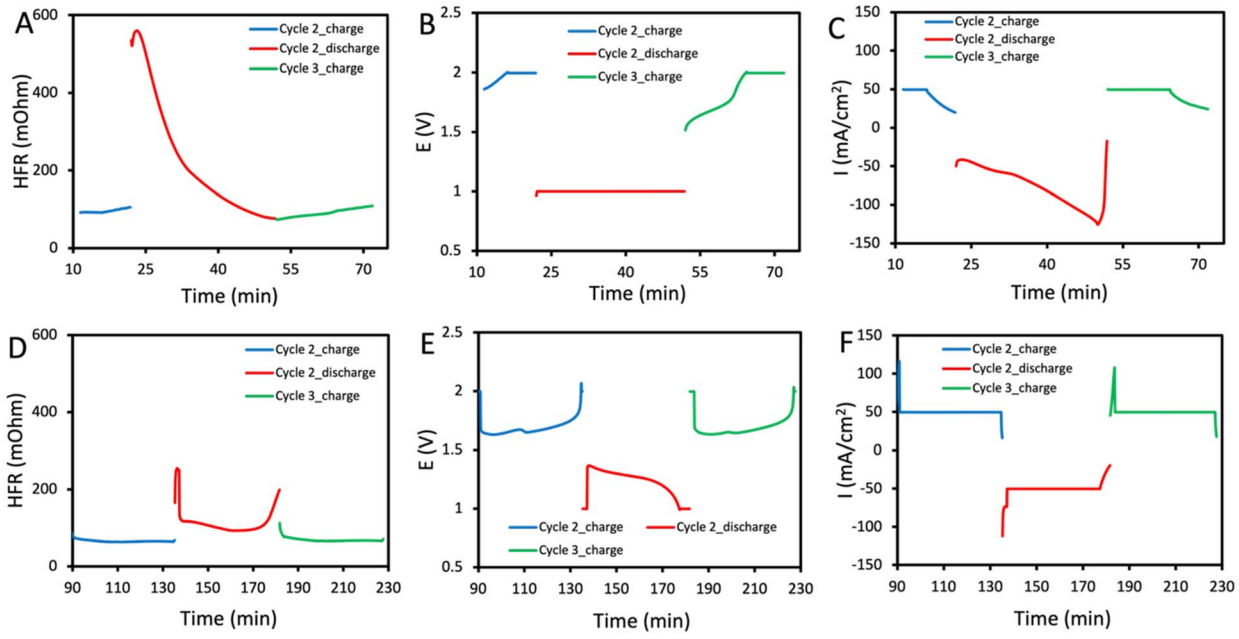

Fig. 4 Ti–Ce RFBs tests: (A) HFR, (B) cell voltage, and (C) current density with a constant-current + constant-voltage protocol; and (D) HFR, (E) cell voltage, and (F) current density with a constant-voltage + constant-current + constant-voltage protocol. Catholyte: 1.23 M $Ce(SO_4)_2$ in 1.05 M AS and anolyte: 1.23 M $TiOSO_4$ in 1.9 M AS after a full reduction to Ti(III).

tabulated in the SI Appendix, Table S5, and the values were comparable with electrolytes of other RFBs.[50] Thus, the increase in HFR was traced back to the structure of the Ce(IV) complex in solution. As discussed earlier, Ce(IV) was bound with HSO_4^- to form a complex that is much larger than HSO_4^-. Since an AEM was used in RFB tests, the transport of negative charge through the separator was required to maintain electroneutrality. Nonetheless, the substantial steric bulk and local positive charge of Ce(IV) would hamper this process, resulting in a high HFR. To discuss the effects of this complex on electrochemical reaction kinetics, the solvent reorganization energy, λ, which is the amount of energy required to re-organize the solvent configuration of the reactant to the state of the product, was calculated using eqn (9).[55] In this equation, α is the electron transfer coefficient, F is Faraday's constant (96 485 C mol^{-1}), E_0 is the standard potential of the considered reaction, which is the average of anodic and cathodic peak potential in CV, and ϕ_r is the potential at the plane of the reaction site *versus* the bulk solution. Since the reaction was assumed to occur at the surface of the electrode, $E \approx \phi_r$. Taking the CV of 10 mV s^{-1} in Fig. 3C as an example, where α_c was 0.209 and E_0 was 1.1 V, the corresponding solvation overpotential, λ/F, was calculated to be 0.945 V. Given that the difference between the maximum applied potential (2 V) and E_0 was less than the solvation overpotential, the Ce complex is unlikely to be desolvated, indicating that the Ce(IV) complex was undergoing an outer-sphere electron transfer. In other words, the active redox couple at the positive electrode consisted of Ce complexes with different oxidation states rather than desolvated Ce^{4+} and Ce^{3+}. The fact that the active species was in a bulky complex form also explains the steric bulk inducing high HFR. As the discharge advanced, more Ce(IV) was reduced to Ce(III) and free HSO_4^- was gradually released owing to the deficiency of Ce(III) in complexing with sulfate. Consequently, the HFR fell as the ionic charge carrier changed from the Ce(IV) complex to the far less bulky HSO_4^- ion. This postulation successfully correlates the HFR behavior with the proposed Ce(IV) structure in AS solution.

$$\alpha = 0.5 + \frac{F}{4\lambda}(E - E_0 - \phi_r). \quad (9)$$

To ensure that the majority of the discharge was concentrated in the constant-current phase, a short (2 min) constant-voltage (CV) step of 2 V was added before the constant-current segment with the intention of attenuating the HFR so that the following constant-current stage was terminated by mass transport polarization instead of ohmic polarization. As depicted in Fig. 4E and F, a discharge curve dominated by a constant-current phase was achieved with this new protocol, and the test showed an average EE of 70.2% and was operated consistently for more than 12 h. No second plateau was observed in Fig. 4E, further supporting that V was not crossing into the Ti side during the pre-charging of the V–Ti cell. The move from a typical CC–CV to a CV–CC–CV discharge profile is expected to have minimal impact on eventual grid integration. Grid applications require constant AC power output with frequency matching.[56–59] The battery management system (BMS) and the

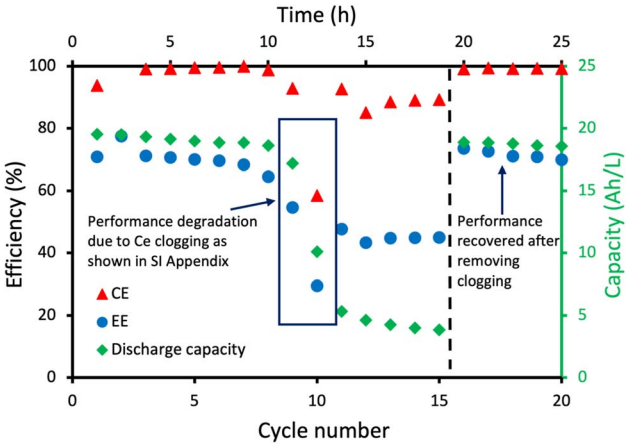

Fig. 5 Ti–Ce RFB performance with a constant-voltage + constant-current + constant-voltage protocol with clogging removed after the 15th cycle. The capacity fading between cycles 8 and 16 was reversible and due to the clogging of the cell tubing and electrode pores by the Ce precipitate, as seen in the ESI Fig. S12. The original capacity was recovered once the precipitates were washed off into the electrolyte tanks. Catholyte: 1.23 M $Ce(SO_4)_2$ in 1.05 M AS and anolyte: 1.23 M $TiOSO_4$ in 1.9 M AS after a full reduction to Ti(III).

power conditioning system (PCS) are designed to ensure this and account for the typical constant DC current-constant DC voltage discharge profiles of batteries. The power conditioning systems coupled to a battery typically incorporate a DC–DC converter to ensure that the DC voltage output from the battery is within the optimal input range for the DC-to-AC converter. The AC output is, in turn, subject to a grid following (GFL) or grid forming (GFM) control scheme.[60] Thus, these systems will ensure that the AC output to the grid will be within acceptable parameters, even when a portion of the discharge happens at a constant DC voltage. After that, both EE and discharge capacity degraded due to the clogging of the tube and flow-field channel induced by Ce precipitation (SI Appendix, Fig. S12). The Ce precipitation was also detected in the CF electrode; the weight of CF after the cycling test was nearly doubled (SI Appendix, Table S6), and clear Ce deposition on graphite fiber was observed by scanning electron microscopy (SEM) and energy dispersive X-ray (EDX) (SI Appendix, Fig. S13 and S14). However, if the precipitate and clogging inside the cell and tube were removed, the performance degradation would be entirely reversed, as shown in Fig. 5, proving that the performance degradation was mainly caused by clogging and not by other modes of irreversible capacity fading. The entrance and exit of flow field in this study was already enlarged compared with the conventional design (Fig. S1A), and the RFB test with the conventional flow field was not even able to finish a typical cycle, as shown in Fig. S15. Future work will focus on other strategies to prevent battery failure from clogging (*e.g.*, by increasing channel widths of flow field and porosity of electrodes). Although the cycling performance shown here was worse than in our previous study using non-AS supporting electrolytes,[51,54] the high theoretical energy density (33.0 Ah L^{-1}) still indicates great potential for further development and

application. Some alternative positive electrodes, *e.g.*, Pt–Ti, will also be tested in future work to examine the role of the oxidative nature of Ce(IV) on the performance of the system. Notably, we have demonstrated diurnal cycling and cycling over several months using carbon felt-based positive electrodes with no deleterious effects.[12,51,54] The oxidative nature of Ce(IV) may even sustain catalytic oxygen functional groups on the positive electrode surface (originally generated by thermal treatment).

Conclusions

The application of the Ce redox couple in RFBs is restricted by the low solubility of Ce. In this work, we developed a supersaturated Ce(IV) electrolyte with 1.23 M active species enabled by an ammonium sulfate-supported electrolyte. Complementary Ce(IV) hydrolysis and complexation were determined to be the primary factors contributing to this high solubility. In the AS solution, Ce(IV) was highly hydrolyzed with water to release protons, which reduced the pH and assisted in the formation of HSO_4^-, and the strong complexation between Ce(IV) and HSO_4^- resulted in a stable structure, proposed as $[Ce(OH)_4(HSO_4^-)_3]^{3-}$. Notably, the operating current density and associated energy efficiency are higher than comparable cerium-based flow batteries observed in previous studies,[11] while simultaneously operating with a 40% higher Ce specific energy. Ti–Ce RFBs based on this electrolyte exhibited very high specific capacity (practically achieved 19 Ah L^{-1} out of a nominal capacity of 33.0 Ah L^{-1}), energy efficiency over 70%, and no irreversible capacity fading, thus making the case for its use in grid-scale energy storage.

Author contributions

JX: conceptualization, data curation, formal analysis, investigation, methodology, validation, visualization, writing-original draft, and writing-review and editing; SS: conceptualization, formal analysis, methodology, writing-original draft, and writing-review and editing; JGC: data curation, writing-original draft, and writing-review and editing; VR: conceptualization, formal analysis, funding acquisition, methodology, project administration, resources, supervision, validation, visualization, writing-original draft, and writing-review and editing.

Conflicts of interest

The authors currently have no financial interests that may be perceived to influence the conclusions presented in this work. Some of the authors are seeking intellectual property protections on aspects of one or more technologies described in this report through the Office of Technology and Management (OTM) at Washington University in St. Louis (WUSTL).

Data availability

All data associated with these studies are represented in the manuscript and its supplementary information (SI). The raw data are available from the corresponding author upon reasonable request. Supplementary information is available. See DOI: https://doi.org/10.1039/d6ta01059h.

Acknowledgements

JX, SS, and VR would like to acknowledge the support of the Advanced Research Projects Agency-Energy (ARPA-E), the US Department of Energy, under the award no. DE-AR0000768 as a part of the Integration and Optimization of Novel Ion Conducting Solids (IONICS) program and the McKelvey School of Engineering, Washington University in St. Louis, and the Roma B. & Raymond H. Wittcoff Distinguished University Professorship. Yin-Yuan Huang is thanked for assistance with the Raman spectroscopy measurement. The work of JGC was supported by the U.S. Department of Energy, Office of Science, Office of Basic Energy Sciences, Critical Minerals and Materials program, under the Award Number DE-SC0022213. Elaine Flynn is thanked for assistance with sample preparation for the XANES analysis.

References

1 M. Shoaib, P. Vallayil, N. Jaiswal, P. I. V. Suba, S. Sankararaman, K. Ramanujam and V. Thangadurai, Advances in redox flow batteries - A comprehensive review on inorganic and organic electrolytes and engineering perspective, *Adv. Energy Mater.*, 2024, **14**, 2400721.
2 Z. Hou, X. Chen, J. Liu, Z. Huang, Y. Chen, M. Zhou, W. Liu and H. Zhou, Towards a high efficiency and low-cost aqueous redox flow battery: A short review, *J. Power Sources*, 2024, **601**, 234242.
3 R. Huang, S. Liu, Z. He, W. Zhu, G. Ye, Y. Su, W. Deng and J. Wang, Electron-deficient sites for improving V^{2+}/V^{3+} redox kinetics in vanadium redox flow batteries, *Adv. Funct. Mater.*, 2022, **32**, 2111661.
4 V. Fernandez, Rare-earth elements market: A historical and financial perspective, *Resour. Policy*, 2017, **53**, 26–45.
5 S. Fahed, R. Pointecouteau, M. Aouine, A. Boréave, S. Gil, V. Meille, P. Bazin, O. Toulemonde, A. Demourgues, M. Daturi and P. Vernoux, Pr-rich cerium-zirconium-praseodymium mixed oxides for automotive exhaust emission control, *Appl. Catal., A*, 2022, **644**, 118800.
6 T. S. Lima, M. C. Santos and A. J. Motheo, Electrochemical generation of hydrogen peroxide using cerium oxide nanostructures supported on graphene: Synthesis, characterization, and application in wastewater treatment, *Electrochim. Acta*, 2025, **521**, 145931.
7 L. C. Chen, T. Luo, Z. Y. Cao, P. Dalladay-Simpson, G. Huang, D. Peng, L. L. Zhang, F. A. Gorelli, G. H. Zhou, H. Q. Lin and X. J. Chen, Synthesis and superconductivity in yttrium-cerium hydrides at high pressures, *Nat. Commun.*, 2024, **15**, 1809.
8 P. Wei, Y. Wang, H. Feng, F. Zhang, Z. Ji, K. Zhang, Q. Zhang, L. Jiang, Y. Qian and Y. Fu, Gene-engineered cerium-exosomes mediate atherosclerosis therapy through remodeling of the inflammatory microenvironment and DNA damage repair, *Small*, 2024, **20**, 2404463.

9 M. Shahbaz, S. Sharif, A. Shahzad, Z. S. Şahin, B. Riaz and S. Shahzad, Enhanced electrochemical performance of cerium-based metal organic frameworks derived from pyridine-2,4,6-tricarboxylic acid for energy storage devices, *J. Energy Storage*, 2024, **88**, 111463.
10 Z. Xie, Q. liu, Z. Chang and X. Zhang, The developments and challenges of cerium half-cell in zinc–cerium redox flow battery for energy storage, *Electrochim. Acta*, 2013, **90**, 695–704.
11 L. F. Arenas, F. C. Walsh and C. P. De León, Zinc–cerium and related cerium-based flow batteries: Progress and challenges, in *Flow Batteries*, ed C. Roth, J. Noack and M. Skyllas-Kazacos, Wiley, 1st edn, 2003.
12 S. Sankarasubramanian, Y. Zhang and V. Ramani, Methanesulfonic acid-based electrode-decoupled vanadium–cerium redox flow battery exhibits significantly improved capacity and cycle life, *Sustainable Energy Fuels*, 2019, **3**, 2417–2425.
13 F. C. Walsh, C. P. de Léon, L. Berlouis, G. Nikiforidis, L. F. Arenas-Martínez, D. Hodgson and D. Hall, The development of Zn–Ce hybrid redox flow batteries for energy storage and their continuing challenges, *ChemPlusChem*, 2015, **80**, 288–311.
14 A. Paulenova, S. E. Creager, J. D. Navratil and Y. Wei, Redox potentials and kinetics of the Ce^{3+}/Ce^{4+} redox reaction and solubility of cerium sulfates in sulfuric acid solutions, *J. Power Sources*, 2002, **109**, 431–438.
15 R. M. Spontnitz, R. P. Kreh, J. T. Lundquist and P. J. Press, Mediated electrosynthesis with cerium (IV) in methanesulphonic acid, *J. Appl. Electrochem.*, 1990, **20**, 209–215.
16 Y. Li, P. Geysens, X. Zhang, J. Sniekers, J. Fransaer, K. Binnemans and I. F. J. Vankelecom, Cerium-containing complexes for low-cost, non-aqueous redox flow batteries (RFBs), *J. Power Sources*, 2020, **450**, 227634.
17 E. S. Beh, D. D. Porcellinis, R. L. Gracia, K. T. Xia, R. G. Gordon and M. J. Aziz, A neutral pH aqueous organic–organometallic redox flow battery with extremely high capacity retention, *ACS Energy Lett.*, 2017, **2**, 639–644.
18 L. Y. Cao, M. Skyllas-Kazacos, C. Menictas and J. Noack, A review of electrolyte additives and impurities in vanadium redox flow batteries, *J. Energy Chem.*, 2018, **27**, 1269–1291.
19 M. Skyllas-Kazacos, C. Peng and M. Cheng, Evaluation of precipitation inhibitors for supersaturated vanadyl electrolytes for the vanadium redox battery, *Electrochem. Solid-State Lett.*, 1999, **2**, 121–122.
20 N. Kausar, A. Mousa and M. Skyllas-Kazacos, The effect of additives on the high-temperature stability of the vanadium redox flow battery positive electrolytes, *ChemElectroChem*, 2016, **3**, 276–282.
21 N. W. Pettinger, R. E. A. Williams, J. Q. Chen and B. Kohler, Crystallization kinetics of cerium oxide nanoparticles formed by spontaneous, room-temperature hydrolysis of cerium(IV) ammonium nitrate in light and heavy water, *Phys. Chem. Chem. Phys.*, 2017, **19**, 3523–3531.
22 C. A. Buchanan, D. Herrera, M. Balasubramanian, B. R. Goldsmith and N. Singh, Unveiling the cerium(III)/(IV) structures and charge-transfer mechanism in sulfuric acid, *JACS Au*, 2022, **2**, 2742–2757.
23 E. P. Jahrman, W. M. Holden, A. S. Ditter, D. R. Mortensen, G. T. Seidler, T. T. Fister, S. A. Kozimor, L. F. J. Piper, J. Rana, N. C. Hyatt and M. C. Stennett, An improved laboratory-based x-ray absorption fine structure and x-ray emission spectrometer for analytical applications in materials chemistry research, *Rev. Sci. Instrum.*, 2019, **90**, 024106.
24 B. Ravel and M. Newville, ATHENA, ARTEMIS, HEPHAESTUS: data analysis for X-ray absorption spectroscopy using IFEFFIT, *J. Synchrotron Radiat.*, 2005, **12**, 537–541.
25 M. Newville, IFEFFIT : interactive XAFS analysis and FEFF fitting, *J. Synchrotron Radiat.*, 2001, **8**, 322–324.
26 R. S. Nicholson and I. Shain, Theory of stationary electrode polarography: Single scan and cyclic methods applied to reversible, irreversible, and kinetic systems, *Anal. Chem.*, 1964, **36**, 706–723.
27 R. S. Nicholson, Theory and application of cyclic voltammetry for measurement of electrode reaction kinetics, *Anal. Chem.*, 1965, **37**, 1351–1355.
28 R. J. Klingler and J. K. Kochi, Electron-transfer kinetics from cyclic voltammetry. Quantitative description of electrochemical reversibility, *J. Phys. Chem.*, 1981, **85**, 1731–1741.
29 S. Yun, J. Parrondo and V. Ramani, Derivatized cardo-polyetherketone anion exchange membranes for all-vanadium redox flow batteries, *J. Mater. Chem. A*, 2014, **2**, 6605–6615.
30 A. M. Shahin, F. Grandjean, G. J. Long and T. P. Schuman, Cerium L_{III}-Edge XAS investigation of the structure of crystalline and amorphous cerium oxides, *Chem. Mater.*, 2005, **17**, 315–321.
31 P. Nachimuthu, W.-C. Shih, R.-S. Liu, L.-Y. Jang and J.-M. Chen, The study of nanocrystalline cerium oxide by X-Ray absorption spectroscopy, *J. Solid State Chem.*, 2000, **149**, 408–413.
32 H. Yoshida, L. Yuliati, T. Hamajima and T. Hattori, Valence of highly dispersed cerium oxide species on silica quantitatively estimated by Ce L_{III}-edge XANES, *Mater. Trans.*, 2004, **45**, 202–2067.
33 C. A. Buchanan, E. Ko, S. Cira, M. Balasubramanian, B. R. Goldsmith and N. Singh, Structures and free energies of cerium ions in acidic electrolytes, *Inorg. Chem.*, 2020, **59**, 12552–12563.
34 Y. H. Zhang and C. K. Chan, Understanding the hygroscopic properties of supersaturated droplets of metal and ammonium sulfate solutions using Raman spectroscopy, *J. Phys. Chem. A*, 2002, **106**, 285–292.
35 Y. H. Zhang and C. K. Chan, Study of contact ion pairs of supersaturated magnesium sulfate solutions using Raman scattering of levitated single droplets, *J. Phys. Chem. A*, 2000, **104**, 9191–9196.
36 L. F. Arenas, C. Ponce de León and F. C. Walsh, Electrochemical redox processes involving soluble cerium species, *Electrochim. Acta*, 2016, **205**, 226–247.

37 W. Schmickler, R. R. Nazmutdinov, Q. Wang and W. A. Daoud, Electrochemistry of Ce(IV)/Ce(III) redox couples in mixed solutions for aqueous flow battery: Experimental and molecular modelling study, *Electrochim. Acta*, 2021, **368**, 137601.

38 M. A. Brown, A. Paulenova and A. V. Gelis, Aqueous complexation of thorium(IV), uranium(IV), neptunium(IV), plutonium(III/IV), and cerium(III/IV) with DTPA, *Inorg. Chem.*, 2012, **51**, 7741–7748.

39 R. Marsac, F. Réal, N. L. Banik, M. Pédrot, O. Pourret and V. Vallet, Aqueous chemistry of Ce(IV): estimations using actinide analogues, *Dalton Trans.*, 2017, **16**, 13553–13561.

40 S. A. Hayes, P. Yu, T. J. O'Keefe, M. J. O'Keefe and J. O. Stoffer, The phase stability of cerium species in aqueous systems: I. E-pH diagram for the system, *J. Electrochem. Soc.*, 2002, **149**, C623–C630.

41 B. Bouchaud, J. Balmain, G. Bonnet and F. Pedraza, pH-distribution of cerium species in aqueous systems, *J. Rare Earths*, 2012, **30**, 559–562.

42 Q. Sun, The Raman OH stretching bands of liquid water, *Vib. Spectrosc.*, 2009, **51**, 213–217.

43 M. Jordanov and R. Zellner, Investigations of the hygroscopic properties of ammonium sulfate and mixed ammonium sulfate and glutaric acid micro droplets by means of optical levitation and Raman spectroscopy, *Phys. Chem. Chem. Phys.*, 2006, **8**, 2759–2764.

44 M. Park, E. S. Beh, E. M. Fell, Y. Jing, E. F. Kerr, D. D. Porcellinis, M. A. Goulet, J. Ryu, A. A. Wong, R. G. Gordon, J. Cho and M. J. Aziz, A high voltage aqueous zinc–organic hybrid flow battery, *Adv. Energy Mater.*, 2019, **9**, 1900694.

45 A. J. Bard and L. R. Faulkner, *Electrochemical Methods: Fundamentals and Applications*, Wiley, 2nd edn, 2000.

46 C. O. Laoire, S. Mukerjee, K. M. Abraham, E. J. Plichta and M. A. Hendrickson, Influence of nonaqueous solvents on the electrochemistry of oxygen in the rechargeable lithium-air battery, *J. Phys. Chem. C*, 2010, **114**, 9178–9186.

47 Y. A. Gandomi, D. S. Aaron, J. R. Houser, M. C. Daugherty, J. T. Clement, A. M. Pezeshki, T. Y. Ertugrul, D. P. Moseley and M. M. Mench, Critical review—Experimental diagnostics and material characterization techniques used on redox flow batteries, *J. Electrochem. Soc.*, 2018, **165**, A910–A1010.

48 Y. Li, J. Bao, M. Skyllas-Kazacos, M. P. Akter, X. Zhang and J. Fletcher, Studies on dynamic responses and impedance of the vanadium redox flow battery, *Appl. Energy*, 2019, **237**, 91–102.

49 K. Amini, A. N. Shocron, M. E. Suss and M. J. Aziz, Pathways to high-power-density redox flow batteries, *ACS Energy Lett.*, 2023, **8**, 3526–3535.

50 L. Tang, P. Leung, Q. Xu, M. R. Mohamed, S. Dai, X. Zhu, C. Flox and A. A. Shah, Future perspective on redox flow batteries: aqueous versus nonaqueous electrolytes, *Curr. Opin. Chem. Eng.*, 2022, **37**, 100833.

51 J. Xie, S. Sankarasubramanian and V. Ramani, Asymmetric electrode configurations enhance operating power density and energy efficiency of an aqueous, electrode-decoupled titanium–cerium redox flow battery, *Sustainable Energy Fuels*, 2026, **10**, 1147–1164.

52 S. Sankarasubramanian and V. Ramani, Redox flow battery, *US Pat.*, 11177497, 2021.

53 Z. Wang, S. Sankarasubramanian, V. Ramani, Y. Zhang and J. Parrondo, Doped anion exchange membranes (AEMs) for highly selective separators in electrochemical devices, *US Pat.*, 12521758, 2026.

54 S. Sankarasubramanian, Y. Zhang, C. He, T. Gregory and V. Ramani, *An Aqueous, Electrode-Decoupled Redox-Flow Battery for Long Duration Energy Storage*, 2021, DOI: DOI: 10.21203/rs.3.rs-150474/v1.

55 J.-M. Savéant and D. Tessier, Potential dependence of the electrochemical transfer coefficient. Reduction of some nitro compounds in aprotic media, *J. Phys. Chem.*, 1977, **81**, 2192–2197.

56 M. T. Lawder, B. Suthar, P. W. C. Northrop, S. De, C. M. Hoff, O. Leitermann, M. L. Crow, S. Santhanagopalan and V. R. Subramanian, Battery Energy Storage System (BESS) and Battery Management System (BMS) for Grid-Scale Applications, *Proc. IEEE*, 2014, **102**, 1014–1030.

57 V. Scaini, P. J. Lex, T. W. Rhea and N. H. Clark, *Battery energy storage for grid support applications*, 2002, https://www.sandia.gov/ess-ssl/EESAT/2002_papers/00002.pdf.

58 Y. Cao, S. B. Lee, V. R. Subramanian and V. M. Zavala, Multiscale model predictive control of battery systems for frequency regulation markets using physics-based models, *J. Process Control*, 2020, **90**, 46–55.

59 C. L. Nge, I. U. Ranaweera, O.-M. Midtgård and L. Norum, A real-time energy management system for smart grid integrated photovoltaic generation with battery storage, *Renewable Energy*, 2019, **130**, 774–785.

60 X. Gao, D. Zhou, A. Anvari-Moghaddam and F. Blaabjerg, A Comparative Study of Grid-Following and Grid-Forming Control Schemes in Power Electronic-Based Power Systems, *PEAD*, 2023, **8**, 1–20.

